Carbon 139 (2018) 913–921

Contents lists available at ScienceDirect

Carbon

journal homepage: www.elsevier.com/locate/carbon

Oxidation limited thermal boundary conductance at metal-graphene interface

David B. Brown [a, *], Thomas L. Bougher [a], Baratunde A. Cola [a, b], Satish Kumar [a]

[a] G. W. Woodruff School of Mechanical Engineering, Georgia Institute of Technology, Atlanta, GA, USA
[b] School of Materials Science and Engineering, Georgia Institute of Technology, Atlanta, GA, USA

ARTICLE INFO

Article history:
Received 11 May 2018
Received in revised form
18 July 2018
Accepted 1 August 2018
Available online 3 August 2018

ABSTRACT

Thermal management is a substantial challenge in high-power-density micro- and nanoelectronic devices, and the thermal resistance at the interfaces in these devices is a major bottleneck to heat removal. Graphene has emerged as a potential candidate for next generation nanoelectronic devices because of its exceptional transport properties; however, the thermal interaction between graphene and other materials such as metals is not completely understood. Here we report thermal boundary conductance (TBC) measurements at metal-graphene-metal (M-G-M) interfaces at room temperature using time-domain thermoreflectance. The metals used in this study represent two classes based on the type of bonding formed with graphene. Ti and Ni form chemisorbed interfaces (strong bonding) with graphene and high TBC is expected while Au forms physisorbed interfaces (weak bonding). The measured TBC at M-G-M interfaces showed little variation (~30 MW/m^2-K) and was similar to metal-graphene-SiO_2 interfaces, contrary to high TBC predicted by previous simulation studies. X-ray photoelectron spectroscopy was used to estimate thickness of the native oxide layer of bottom Ti (2.8 nm) and Ni (2.5 nm) layers. The conductance of these thin native oxide layer was much greater than the overall TBC but prevented formation of chemisorbed interfaces between graphene and metal for Ti and Ni cases leading to significantly lower TBC and highlighting an important consideration for practical applications.

1. Introduction

Graphene, a single-layer of sp^2 bonded C atoms, has been studied extensively since its fabrication was made practical by mechanical exfoliation from highly-ordered pyrolytic graphite (HOPG) [1]. It has attracted immense interest because of its exceptional electrical and thermal transport properties such as high intrinsic carrier mobility [2–5] and thermal conductivity [6–8] making it a potential candidate for applications in next generation nanoelectronic devices. While there is a plethora of literature on electrical characterization of graphene in applications such as graphene field-effect transistors (G-FETS) [9,10] and optoelectronic devices [11,12], the thermal interaction between graphene and the metals/insulators has received much less attention until recently. Heat removal in short channel G-FETS may be limited by metal-graphene (M-G) interfaces [13,14] causing localized heating which can have a detrimental effect on performance and reliability of these devices. The thermal boundary conductance (TBC), or Kapitza conductance [15,16], is typically used to quantify the effectiveness of an interface at transporting thermal energy. Fundamental understanding of thermal transport at these interfaces is essential for the commercial application of these devices [17].

The M-G interaction is a mixture of covalent, ionic, and van der Waals interactions [18]. Metals have been categorized into two groups, weak adsorption (physisorption) and strong adsorption (chemisorption) [19–21], based on their interfacial interaction strength with graphene. Interfaces between graphene and metals such as Ni, Co, Cr, Pd, and Ti result in chemisorption, which perturbs the electronic band structure of graphene due to hybridization of graphene π-bands with metal d-bands. These are favored over metals such as Cu, Al, Ag, Ir, Au, and Pt which result in physisorption. At physisorbed interfaces, the graphene electronic band structure is preserved; however, significant charge transfer may occur from metal to graphene, or vice versa, depending on the

* Corresponding author. G. W. Woodruff School of Mechanical Engineering, Georgia Institute of Technology, 771 Ferst Drive, Love Manufacturing Building, 30332, Atlanta, GA, USA.
E-mail address: dbrown3@gatech.edu (D.B. Brown).

https://doi.org/10.1016/j.carbon.2018.08.002
0008-6223/

Nomenclature

d	layer thickness (nm)
D	thermal diffusivity (m^2/s)
f	modulation frequency (MHz)
k	thermal conductivity (W/m-K)
L	thermal penetration depth (m)
L_K	Kapitza length (m)
L_0	Lorenz number ($W\Omega/K^2$)
TBC	thermal boundary conductance (MW/m^2-K)
V_{in}/V_{out}	ratio of in-phase to out-of-phase signal of the lock-in amplifier

differences in work function causing a shift in graphene Fermi level and the formation of an interface dipole layer. The graphene becomes n-type (Cu, Al, Ag, Ni, Co, Pd, Ti) or p-type (Au, Pt) doped depending on the selection of metal contacts and can be used to create p-n junctions [22,23]. However, the thermal transport at the M-G interface has been attributed to phonons [24–26]. The M-G interaction has also been shown to affect the phonon dispersion of graphene [27–31], with more pronounced changes for chemisorbed interfaces (Ni, Ti) compared to physisorbed (Au, Cu, Pt). Allard and Wirtz [29] used density functional theory (DFT) to show that adsorption of graphene on Ni led to softening of longitudinal, transverse, and out-of-plane optical (LO, TO, and ZO) modes and a gap opening between branches for out-of-plane optic and acoustic (ZO and ZA) modes at the K point of the Brillouin zone indicating the graphene had adsorbed onto the Ni substrate. Mode softening of LO, TO, and ZO modes and the gap opening between ZO and ZA modes at the K point was observed experimentally using high-resolution electron-energy loss spectroscopy (HREELS) confirming the change in phonon properties of graphene due to the interactions with metals [27,32].

Previous studies have shown that M-G-M sandwiched structure may enhance the M-G interface interaction. Gong et al. [33] varied the top and bottom metals in an effort to improve the interface interaction between graphene and physisorbed metals. The result was increased binding energy at Cu-, Ag-, Ir-, Au-, and Pt-G interfaces, which was attributed to different interface dipoles being formed at the top and bottom M-G interfaces. Franklin et al. [34], using 25 nm Pd-5 nm Ti as the bottom metal and 30 nm Au-30 nm Pd-0.5 nm Ti as the top metal, showed a reduction in electrical contact resistance (~40%). This was attributed to enhanced M-G coupling and higher graphene doping. Liang et al. [31] using DFT, showed a significant change in the phonon DOSs of single-layer graphene (SLG) sandwiched between Ti layers, which was attributed to strong interactions of SLG with Ti (chemisorbed) compared to Cu and Au (physiorbed). This resulted in much higher TBC, calculated using DFT along with the atomistic Green's function (AGF) method, at Ti-SLG-Ti interface compared to Au-SLG-Au and Cu-SLG-Cu interfaces. Mao et al. [35] also showed increased TBC at chemisorbed Ni-SLG interface compared to physisorbed Au- and Cu-SLG using first-principles calculations. To date there has been no experimental evidence as to whether certain metals can enhance the TBC based on their interactions with graphene.

Time domain thermoreflectance (TDTR) has become a popular technique for measuring thermal conductivity and TBC in thin films and substrates. TDTR has also been used to measure TBC at M-HOPG [36,37], M-G-SiO_2 [24,38–42], and M-G-M interfaces [25,26,43,44]. Schmidt et al. [36] reported the TBC at Ti-HOPG interface to be three to four times higher than Au-HOPG interface and two to three times higher than Al-HOPG interface, indicating that chemisorbed interfaces can have much higher TBC. The inclusion of a 5 nm Ti adhesion increased TBC at Al-HOPG interface to values comparable to Ti-HOPG interface. Gengler et al. [37] measured TBC at several M-HOPG interfaces and found TBC increased with metal Debye temperature up to ~400 K and remained constant at ~60 MW/m^2-K above 400 K. The M-HOPG studies are insufficient to completely explain the M-G interaction since HOPG is essentially successive graphene layers bonded by van der Waals forces, while isolated graphene must be supported by materials (e.g., SiO_2, metals) with very different vibrational properties, interface structure, and chemical interaction (if any).

Koh et al. [24] reported the TBC at Au-G-SiO_2 (2 nm Ti adhesion layer) interface to be 20–30 MW/m^2-K at room temperature (RT) for 1–10 graphene layers. In the same study, TBC was found to depend weakly on temperature above 100 K suggesting the dominant heat carriers across this interface were acoustic phonons. Hopkins et al. [38] investigated chemically functionalized graphene with oxygen using O_2 plasma in an Al-G-SiO_2 structure [6], and TBC was increased from 30 to 40 MW/m^2-K at RT demonstrating that interfacial bonding plays important role in heat transport across this interface [45]. Foley et al. [40] and Walton et al. [41] also studied the effects of plasma-functionalization of graphene. Foley et al. [40] also observed no enhancement in TBC or electrical contact conductance at Au-G-SiO_2 interface with and without a Ti adhesion layer. The authors attributed this to this limited surface reactivity of the graphene surface, however, this effect was not investigated for additional metals such as Ni or even Cr. Yang et al. [39] used frequency-domain thermoreflectance (FDTR) to create micron-scale maps of TBC as well as in-plane thermal conductance, which was used to determine thermal conductivity of graphene, encased between Ti and SiO_2. The TBC was reported to 20–25 MW/m^2-K at RT for one to seven graphene layers, similar to values at Au-G-SiO_2 interface. The effect of oxidation on transport properties at Ti-G interface has been reported recently by Freedy et al. [42], who showed TBC decreased with increasing oxide composition in a 5 nm Ti film on SiO_2 by varying Ti deposition rate. A similar result was observed at other metal-nonmetal interfaces [46].

Jiang et al. combined X-ray photoelectron spectroscopy (XPS) and TDTR and observed enhanced TBC across Al-G-Cu, Cu-G-Cu, and Pt-G-Cu interfaces through controlled oxidation of graphene [43]. Huang et al. [25] showed that improving conformity of graphene to underlying metal increased TBC across Al-G-Cu interface by 35% despite oxidation of underlying Cu layer. The contribution of electrons across M-G-M interfaces has been the subject of recent literature. Zhang et al. [44] reported an electronic contribution while the temperature-dependence of TBC reported by Huang et al. [26] for Pd-G-Pd seemed to confirm no electronic contribution. Despite numerous studies, the TBC at suspected physisorbed and chemisorbed M-G interfaces has never been directly compared. Here we investigate the effect of physisorption versus chemisorption on the M-G-M interfaces using TDTR, and also observe the effect of native oxide layers. The resulting TBC values were in a similar range as M-G-SiO_2 and M-G-M interfaces with little variation for different metals, which is in contrast with first principle based studies [31,35]. We find native oxide thicknesses of several nm which we propose limits TBC by preventing formation of chemisorbed M-G interface.

2. Experimental methods

2.1. Sample preparation

Graphene transfer was performed using a method similar to [47,48]. SLG grown on Cu foil using chemical vapor deposition (CVD) [49] was spin coated (3000 RPM for 60 s) with PMMA (4%

wt./vol in Toluene) and cured at 180 °C for 1 min. Because graphene grows on both sides of the foil, the bottom of the foil was etched using 30 s O_2 plasma (250 W, 50 sccm, 60 mTorr) to remove the graphene layer. The Cu foil was then etched using ammonium persulfate (5% wt./vol. in DI water) for 3–6 h, or until Cu was completely removed. The resulting PMMA-graphene film was transferred to the surface of the target substrate and allowed to dry in the ambient. The substrates were then coated with an additional layer of PMMA in order to relax the wrinkles in the graphene [47]. Following the second PMMA coating, acetone was used to dissolve the PMMA film leaving only graphene on the surface of the samples. The samples were then annealed at 250 °C in vacuum (5–10 mTorr) for three hours in an attempt to remove residual PMMA [50,51] and improve conformity of graphene to the substrate [25]. This procedure was repeated for each sample used in the study.

The samples used in this study will be referred to as SiO_2, Ti, Ni, and Au samples based upon the layer onto which the graphene is transferred. The following is a brief description of each sample. The SiO_2 sample was created by transferring SLG to 300 nm thermally grown SiO_2 on Si (<100>, $\rho = 4\text{-}7\ \Omega$-cm). Following graphene transfer, the SiO_2 sample was coated with 100 nm Au (including a 2 nm Ti adhesion layer between Au and SiO_2) for TDTR measurements. The Ti, Ni, and Au samples were created by transferring graphene to 812 nm thick Ti, 230 nm thick Ni, and 515 nm Au films on Si using electron-beam evaporation (Denton Explorer). Higher deposition rates of 5 and 3 A/s for Ti and Ni, respectively, were used in an effort to reduce oxidation during deposition [52,53]. The Ti and Ni samples were coated with 60 nm Au and 20 nm Ti and 60 nm Au and 20 nm Ni, respectively, without breaking vacuum, while the Au sample was coated with 80 nm Au, to form the M-G-M interface. The 60 nm Au-20 nm Ti and 60 nm Au-20 nm Ni layers were treated as composite layers [39] since the TBC at metal-metal (M-M) interfaces has been reported to be an order of magnitude higher than at M-semiconductor or M-dielectric interfaces [54,55]. Fig. 1 shows a schematic of the geometry for each of the samples used in this study. The TBC values reported here are equivalent to the total thermal conductance of the M-G-SiO_2 or M-G-M interfaces.

The transducer used for all samples was Au, which precluded the use of picosecond acoustics to determine the transducer thickness since the piezoreflectivity (i.e., the change in reflectance with strain) of Au is small near a wavelength of 800 nm [45].

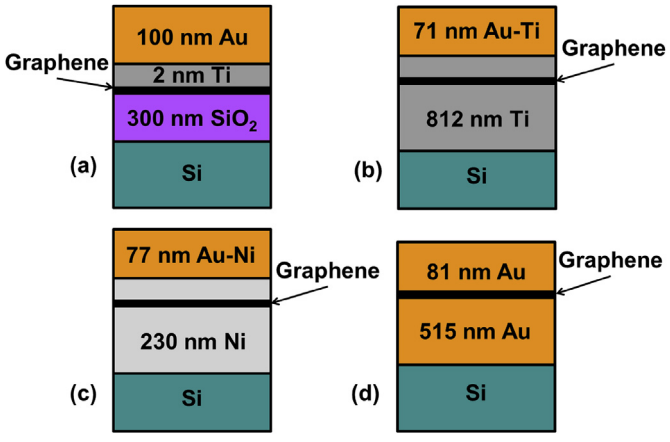

Fig. 1. Schematic of sample geometries used in TDTR measurements. (a) Graphene was transferred to 300 nm thermally grown SiO_2 100 nm and Au transducer (with 2 nm Ti adhesion layer) deposited by e-beam evaporation. Sandwiched graphene structures with (b) 812 nm Ti, (c) 230 nm Ni, and (d) 515 nm Au deposited by e-beam evaporation. Top metal layers for (b), (c), and (d) were 71 nm Au-Ti, 77 nm Au-Ni, and 81 nm Au, respectively. (A colour version of this figure can be viewed online.)

Reference glass slides were co-deposited during each metal deposition in order to determine film thickness and thermal conductivities of the metallic layers. Profilometry (KLA-Tencor P-15) and atomic force microscope (AFM) (Veeco Dimension 3100) measurements performed on reference glass slides were used to determine the height of the thick metal films underneath the graphene interface and the transducer thicknesses (i.e., the metal layer deposited on top of the graphene). The bottom Ti, Ni, and Au films were measured to be 812, 230, and 515 nm thick, respectively, and the Au-Ti, Au-Ni, and Au transducers were 71, 77, and 81 nm thick, respectively. The thermal conductivity of the metal layers was determined by measuring the RT electrical conductivity in conjunction with the Wiedemann-Franz law: $L_0 = k/\sigma T$, where k is thermal conductivity, σ is electrical conductivity, T is absolute temperature, and L_0 is the Lorenz number which is equal to $2.44 \times 10^{-8}\ W\Omega K^{-2}$ [56]. Electrical conductivity measurements were performed on reference glass slides using a four-point probe technique. The metal film thermal conductivities were treated as constants during data fitting, unless otherwise stated. The resulting thermal conductivities of the 812 nm Ti, 230 nm Ni, and 515 nm Au were 6.6, 50, and 200 W/m-K, respectively. The thermal conductivity of the 71 nm Au-Ti and 79 nm Au-Ni composite transducers were measured to be 132 and 131 W/m-K, respectively. The thermal conductivity of the 102 nm Au and 81 nm Au transducers were measured to be 185 and 200 W/m-K, respectively.

2.2. Time-domain thermoreflectance (TDTR)

TDTR is a pump-probe optical technique which uses a modulated laser source (pump) to heat a sample, while an unmodulated laser source (probe) measures the change in optical reflectivity of the surface. The output signal is measured using a lock-in amplifier and the experimental data is fit to a thermal model to extract the thermal properties of the interest. The TDTR setup used in this study is a two-color system which we have described in previous work [57] along with the typical modeling framework [58,59]. Briefly, the output of a Spectra Physics Ti:Sapphire ($\lambda = 800$ nm, 40 nJ/pulse) laser with ~150 fs pulse width and a repetition rate of ~80 MHz is split into two beam paths (pump and probe) where the pump beam is modulated at a frequency of 8.8 MHz and the probe is frequency doubled using a BiBO crystal. The arrival time of the probe is delayed relative to the pump by adjusting its optical length using a double-pass mechanical delay stage in order to map the decay of the thermoreflectance signal. Data fitting was performed using a Levenberg-Marquardt non-linear least squares regression [60] with probe delay times from 0.2 to 7 ns. The $1/e^2$ diameters of the pump and probe beams, measured using a beam profiler (DataRay Inc. Beam'R2), were approximately 40 and 16 μm, respectively, with laser powers of 40–50 mW and 7–10 mW for the pump and probe, respectively. The thermal penetration depth, L, in TDTR measurements is given by,

$$L = \sqrt{D/\pi f} \tag{1}$$

where D is the thermal diffusivity of the sample and f is the modulation frequency [61,62]. Therefore, for a given sample a higher modulation frequency results in lower penetration depth. Lower penetration depth is ideal for the samples in this study due to the location of the interfaces of interest.

In our TDTR measurements, the error from the experimental factors is relatively small compared to the propagation of error from input parameters in the thermal model. This uncertainty is dependent upon the ratio of sensitivity of known and unknown parameters. The sensitivity, S_p, to a parameter, p, in a TDTR

measurement is given by Refs. [62,63],

$$S_p = \frac{\partial \ln(V_{in}/V_{out})}{\partial \ln p} \quad (2)$$

where V_{in}/V_{out} is the ratio of in-phase and out-of-phase signals of the lock-in amplifier. A higher absolute value of sensitivity is desired for accurate data fitting, and we adjust the modulation frequency to achieve the highest sensitivity to the parameters of interest. The measurements in this study were performed at a modulation frequency of 8.8 MHz to provide improved sensitivity to TBC compared to the lower frequencies. We use Monte Carlo (MC) simulations [57,64,65] to estimate the uncertainty of our measurements; these have been shown to be more accurate for low sensitivity parameters, as is the case for interfaces on SiO_2 and Ti samples in this work. The MC simulations include uncertainties due to background noise, error in setting the phase shift of the lock-in amplifier, noise in the measurement signal, and uncertainty in the fixed parameters in the model. Values for each of the uncertain parameters in the model are randomly sampled from a normal distribution to create a set of N initial guess values, while a series of N experimental data sets are created within the experimental uncertainty of the TDTR measurements. The value for N is generally 500–1000. Data fitting is performed on each of the N randomly generated experimental data sets using a single set of the N initial guess values to create a distribution of probable values for TBC of interest. A 90% confidence interval is created by taking the 5th and 95th percentiles as lower and upper bounds, respectively.

3. Results and discussion

3.1. Sensitivity analysis

Fig. 2a shows the sensitivity to various parameters in the measurements performed on the SiO_2 sample, including thickness of the Au transducer layer, d_{Au}, SiO_2 thermal conductivity, k_{SiO2}, and TBC at Au-G-SiO_2 interface, $TBC_{Au-G-SiO2}$. The measurements showed negligible sensitivity to Au transducer thermal conductivity; however, there was significant sensitivity to the thickness of the transducer and SiO_2 thermal conductivity. The sensitivity to TBC was low due to the low thermal conductivity of the SiO_2 layer. This will be discussed in more detail in the next paragraph. In addition to TBC at Ti-G-Ti interface, $TBC_{Ti-G-Ti}$, the measurements on the Ti sample were found to be sensitive to bottom Ti thermal conductivity, k_{Ti}, bottom Ti thickness, d_{Ti}, and Au-Ti transducer thickness, d_{Au-Ti}. The sensitivity of the model to these parameters is shown in Fig. 2b. There was negligible sensitivity to the thermal conductivity of Au-Ti transducer, k_{Au-Ti}. Similar to the SiO_2 sample, the sensitivity to TBC at the Ti-G-Ti interface was low compared to Ni and Au samples due to low thermal conductivity of the bottom Ti layer. The measurements on the Ni and Au samples showed sensitivity to TBC at Ni-Si and Au-Si interfaces, G_{Ni-Si} and G_{Au-Si}, respectively, as well as bottom Ni and Au film thickness, d_{Ni} and d_{Au}, respectively. Sensitivity to the thermal conductivity of Au-Ni and Au transducers, k_{Au-Ni} and k_{Au}, were negligible.

Comparing the Kapitza length [66] ($L_K = \frac{k}{TBC}$) of an interface, where k is the thermal conductivity of the underlying layer, to thickness (d) of the underlying layer, the larger value will limit heat diffusion through the sample resulting in higher sensitivity to the interface or layer in question. For the 812 nm Ti layer with a thermal conductivity of 6.6 W/m-K, the resulting L_K value is 213 nm, using TBC value from Table 1, much lower than the Ti layer thickness. The thermal conductivity of the bottom Ni layer was ~7.5 times higher than the bottom Ti layer, while the thermal conductivity of the bottom Au layer was ~30 times higher. The resulting L_K values of the underlying Ni and Au layers were 1.77 and 6.92 μm, respectively. As a result of the high L_K values, the sensitivity to TBC at Ni-G-Ni and Au-G-Au interfaces was much higher. This is illustrated in Fig. 3 using average TBC values found in this study (Table 1). Fig. 3a compares sensitivity to TBC at M-G-SiO_2 and M-G-M interfaces as a function of delay time. The sensitivity to Au-G-Au interface across this range was higher than M-G-SiO_2 and other M-G-M interfaces as a result of higher L_K. Fig. 3b shows a comparison of sensitivity to TBC at these interfaces for TBC values ranging from 10 to 100 MW/m^2-K at a delay time of 200 ps. We found that it was necessary to fit for thermal conductivity of underlying layer in SiO_2 and Ti samples due to low sensitivity to TBC while these parameters could be held constant in Ni and Au samples.

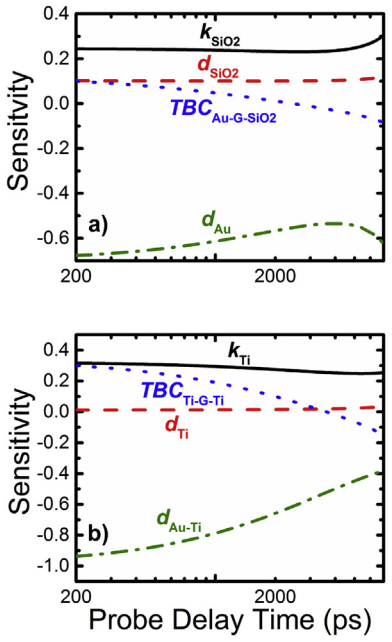

Fig. 2. (a) Sensitivity to thickness of the Au transducer layer (green-dash-dot), d_{Au}, SiO_2 thermal conductivity (black-solid) and thickness (red-dash), k_{SiO2} and d_{SiO2}, respectively, and TBC at Au-G-SiO_2 interface (blue-dot), $TBC_{Au-G-SiO2}$, (b) Sensitivity to various parameters in Ti sample including bottom Ti thermal conductivity (black-solid), k_{Ti}, TBC at Ti-G-Ti interface (blue-dot), $TBC_{Ti-G-Ti}$, bottom Ti thickness (red-dash), d_{Ti}, and Au-Ti transducer thickness (green-dash-dot), d_{Au-Ti}. (A colour version of this figure can be viewed online.)

3.2. Au-graphene-SiO_2

The optical microscope image in Fig. 4a shows a 1 × 1 mm^2 area of SiO_2 coated with graphene. The atomic force microscope image in Fig. 4b shows a typical 1 × 1 μm^2 area on the surface of the SiO_2 sample. There are inherent wrinkles on the graphene surface resulting from the transfer process [48]. We use Raman (Renishaw InVia) and X-ray photoelectron spectroscopy (XPS) (Thermo Scientific K-Alpha$^+$) to verify the presence of SLG on the surface of the

Table 1
Summary of TBC values at M-G-SiO_2 and M-G-M interfaces. Statistical uncertainty analysis (MC simulations) was performed to determine upper/lower uncertainty bounds.

Sample	*TBC* (MW/m^2-K)	Unc. (MW/m^2-K)
Au-G-SiO_2	27.7	+2.9/-2.4
Ti-G-Ti	30.9	+2.9/-2.7
Ni-G-Ni	28.2	+6.2/-9.6
Au-G-Au	28.9	+5.6/-4.5

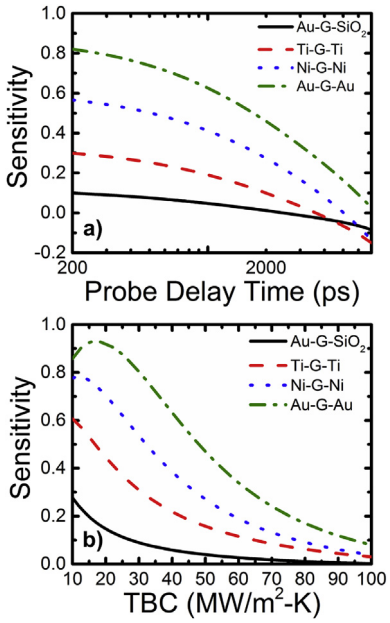

Fig. 3. Comparison of sensitivity of TBC at Au-G-SiO_2 (black-solid), Ti-G-Ti (red-dash), Ni-G-Ni (blue-dot), and Au-G-Au (green-dash-dot) interfaces (a) as a function of delay time and (b) for different TBC values at a delay time of 200 ps.

sample. Fig. 4c shows the resulting Raman spectrum with G peak at ~1591 cm^{-1} and 2D peak ~2678 cm^{-1} and intensity ratio I(2D)/I(G) ≈ 3.1 which is typical of SLG [67]. The D peak at ~1344 cm^{-1} (I(D)/I(G) ≈ 0.15) is indicative of disorder/defects in the graphene layer (pristine graphene would have no D peak) which often arise near the sample edge or grain boundaries in graphite or graphene with small crystallite size [68]. The D peak could also arise due to the presence of sp^3 amorphous carbon [69]. To quantify the disorder in the graphene, we use the relation of Cancado et al. [70] to estimate the distance between defects and defect density of our samples to be~31 nm and $\approx 3.4 \times 10^{10}$ cm^{-2} for an excitation laser wavelength of 532 nm. The large D peak in the graphene samples is higher than some previous studies but comparable to previous TDTR studies on transferred CVD-grown graphene [38]. However, the goal of this study is to compare TBC for different metal-graphene interfaces which we are still able to do since the graphene quality is constant across all samples. Fig. 4d shows the deconvolution of the C1s XPS spectrum with labeled peaks indicating the different types of bonding present in our graphene sample.

The TBC of the SiO_2 sample was measured in areas with and without graphene for comparison. Both TBC and SiO_2 thermal conductivity were used as fitting variables. The resulting SiO_2 thermal conductivity (1.14 W/m-K) was near the bulk value [71]. The average TBC values were 84.9 and 27.7 MW/m^2-K for the Au-SiO_2 and Au-G-SiO_2 interfaces, respectively, which are in agreement with previously reported values [24,40]. The MC method described earlier and discussed in detail in Ref. [57] was used to obtain a better estimate of the lower uncertainty bound compared with analytical expressions [59]. A histogram showing the distribution of TBC values at the Au-G-SiO_2 interface and a convergence plot showing the 5th, 50th, and 95th percentiles from a typical MC simulation are shown in Fig. 5a and b, respectively. The reported TBC values at the Au-SiO_2 and Au-G-SiO_2 interfaces, 84.7 and 27.7 MW/m^2-K, respectively, are the average of the 50th percentiles from each MC simulation. The upper and lower uncertainty bounds, the average of the 95th and 5th percentiles, respectively, were +2.9/-2.4 MW/m^2-K for the Au-G-SiO_2 interface.

3.3. Metal-graphene-metal

The TBC at M-G-M interfaces were in a similar range as the SiO_2 sample. The thermal conductivity of the underlying Ti layer was

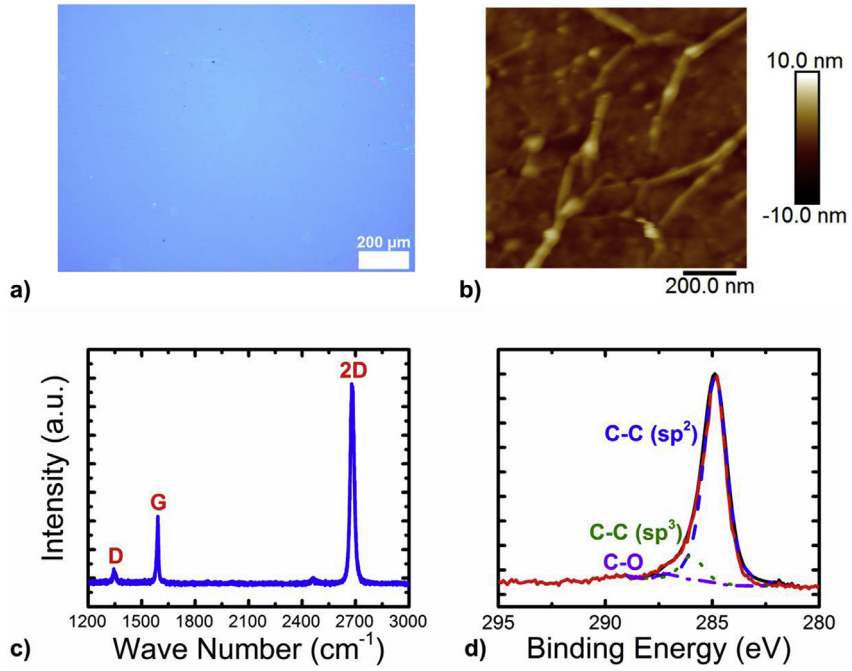

Fig. 4. (a) Optical microscope image of graphene on the surface of 300 nm SiO_2. Image shows graphene covering an area of 1 × 1 mm^2. (b) Atomic force microscope images showing 1 × 1 μm^2 surface of graphene on SiO_2. (c) Raman spectrum for graphene on 300 nm SiO_2 with G peak at ~1591 cm^{-1} and 2D peak at ~2678 cm^{-1}. The relative intensity of the 2D to G peak (I(2D)/I(G) ≈ 3.1) indicates this is SLG, while the D peak at ~1344 cm^{-1} (I(D)/I(G) ≈ 0.15) is related to disorder/defects in the graphene layer. (d) The deconvolution of the C1s XPS spectrum shows the different types of bonding in the graphene layer. (A colour version of this figure can be viewed online.)

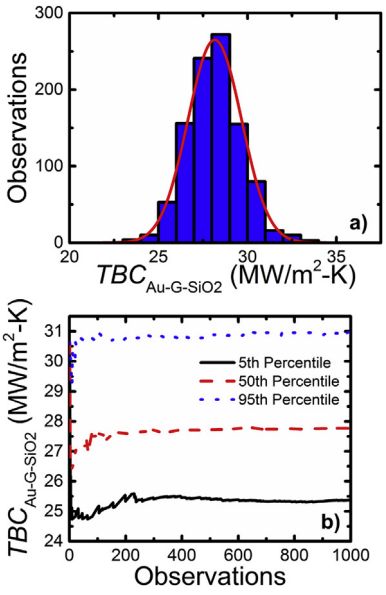

Fig. 5. Results of a typical Monte Carlo simulations for measurements performed on the SiO_2 sample. (a) A histogram showing the distribution of TBC values at Au-G-SiO_2 interface. (b) Convergence plot showing the 5th, 50th, and 95th percentile. The 50th percentile is taken as the TBC value, while the 95th and 5th percentiles represent the upper and lower uncertainty bound, respectively. (A colour version of this figure can be viewed online.)

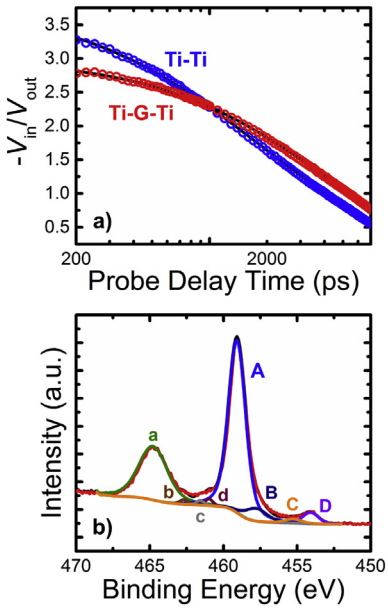

Fig. 6. (a) Comparison of typical data fits for Ti sample. (b) Ti2p XPS spectrum with peaks labeled corresponding to TiO_2 (A and a) and the suboxides Ti_2O_3 (B and b), TiO (C and c), and Ti (D and d). (A colour version of this figure can be viewed online.)

used as a fitting parameter along with TBC at Ti-Ti and Ti-G-Ti interfaces. The resulting data fits are shown in Fig. 6a. The Ti thermal conductivity from TDTR was approximately 9.6 W/m-K, slightly higher than our value of 6.6 W/m-K using the Wiedemann-Franz law which measures the electronic contribution to thermal conductivity. An increased lattice contribution caused by metal oxidation may be the source of the difference in thermal conductivity observed using TDTR [56]. In addition, the Lorenz number, L_0, may differ from the theoretical value (2.44×10^{-8} WΩK^{-2}) for various metals [72] where higher Lorenz numbers can arise from increased lattice contribution. Using the k (9.6 W/m-K) value from TDTR and measurement of σ (9.18×10^5 S/m) from the four-point probe technique to calculate Lorenz number results in a L_0 value of 3.54×10^{-8} WΩK^{-2}. Average TBC values at Ti-Ti and Ti-G-Ti interfaces were 96.1 and 30.9 MW/m^2-K, respectively. The TBC at Ti-Ti interface was an order of magnitude lower than expected for a M-M interface [54,55], which is attributed to oxidation in the Ti layer confirmed using XPS. The effect is analogous to decreased TBC observed at Al-Si interface in the presence of a native oxide layer [73]. The Ti2p XPS spectrum shown in Fig. 6b was used to determine the thickness of the oxide layer following the method of McCafferty and Wightman [74] where the oxide film was modeled as a mixture of TiO_2 and the suboxides Ti_2O_3 and TiO. The ineleastic electron mean free paths were calculated from the NIST Electron Inelastic Mean Free Path Database [75] using the predictive formula of Gries [76] with densities of 4.5, 4.23, 4.49, and 4.95 g/cm^3 for Ti, TiO_2, Ti_2O_3, and TiO, respectively. The total oxide thickness was found to be~2.8 nm with the contribution of each suboxide being 1.3, 1.1, and 0.44 nm for TiO_2, Ti_2O_3, and TiO, respectively. Since graphene forms a chemisorbed interface with Ti, it is possible that the TBC would be higher if Ti oxidation can be prevented in the samples.

The TBC of the Ni-Ni interface was an order of magnitude larger than Ni-G-Ni interface (315 versus 28.2 MW/m^2-K), a larger difference than observed for Ti samples. The resulting data fits for measurements on Ni sample are shown in Fig. 7a. The TBC at Ni-Ni interface was more than three times the TBC at the Ti-Ti interface. Similar to the Ti case, oxidation of Ni layer likely led to lower TBC value at Ni-Ni interface. The Ni2p XPS spectrum is presented in Fig. 7b with main peaks corresponding to Ni, NiO, and $Ni(OH)_2$ [77]. However, unlike Ti, it was not explicitly stated whether the native oxide layer formed on the Ni surface can be treated as a multilayer stack with contributions from each oxidation state. The thickness of the mixed oxide/hydroxide film on the Ni sample, with contributions from NiO and $Ni(OH)_2$, was 2.5 nm estimated using the method of Strohmeier [78–80] of. The sensitivity to TBC at Au-Au interface was extremely low due to the high TBC value at this interface. Gundrum et al. [54] reported TBC at Al-Cu interface to be 4 GW/m^2-K at RT; we expect TBC at Au-Au interface is much higher than this value since Au does not oxidize. Wilson et al. [55] reported TBC of 14 GW/m^2-K at Pd/Ir interface. We believe TBC at this interface is too high to resolve in the current sample configuration, but estimate its value to be > 10 GW/m^2-K based on MC results. The average TBC value at Au-G-Au interface was 28.9 MW/m^2-K. Fig. 7c shows a typical data fit for the Au sample used in this study. A comparison of average TBC values for samples in this study are shown in Fig. 7d and the results are listed in Table 1. The error bars shown in Fig. 7d and the uncertainty values listed in Table 1 were obtained using MC simulations. The two values listed in the uncertainty column, corresponding to the lower and upper uncertainty bounds, are taken as 5th percentile and 95th percentile, respectively.

The TBC results at M-G-M interfaces presented here were found to be in similar range as previously reported M-G-SiO_2 [24,38–42], and M-G-M interfaces [25,26,43,44]. The total native oxide layer thickness estimated from the XPS spectra of Ti and Ni samples was 2.8 and 2.5 nm, respectively. Assuming the thermal conductivity of the oxide layers to be 1 W/m-K, this corresponds to a thermal conductance of 357 and 400 MW/m^2-K for Ti and Ni samples, much higher than measured TBC value at Ti-G-Ti and Ni-G-Ni interfaces, both of which contribute to the total interfacial thermal conductance [81]. Freedy et al. [42] showed increased TBC with decreased oxide concentration for a 5 nm Ti layer for graphene on SiO_2 at the M-G-SiO_2 interface showing that Ti oxidation, as opposed to

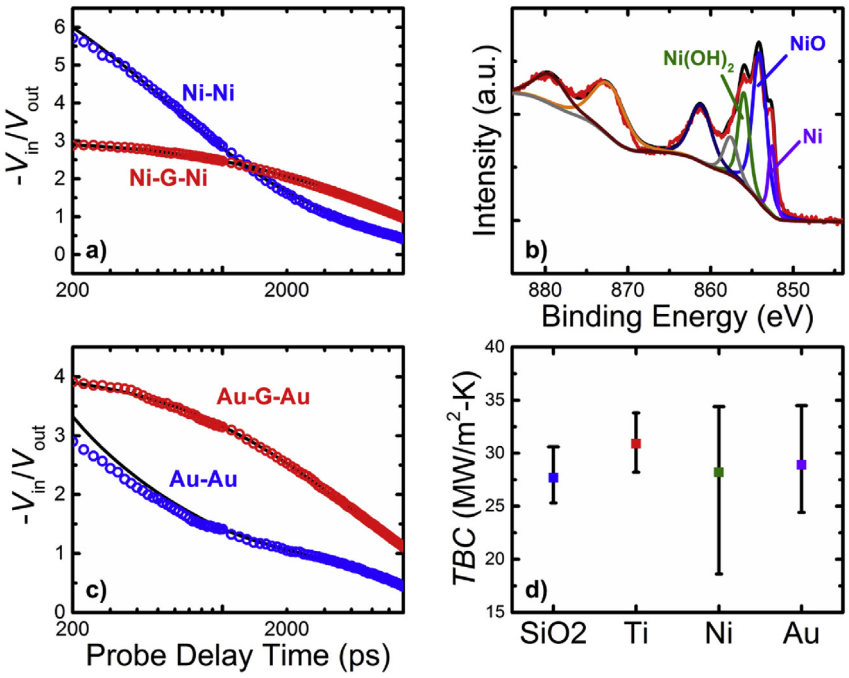

Fig. 7. Typical data fit for (a) Ni and (c) Au samples used in this study. (b) Ni2p XPS spectrum with main peaks associated with Ni, NiO, and $Ni(OH)_2$. (d) Comparison of TBC values at graphene interfaces (e.g. Au-G-SiO_2, Ti-G-Ti) for all samples used in this study (also listed in Table 1). (A colour version of this figure can be viewed online.)

graphene surface reactivity [40], is the limiting factor. A similar observation was made at Au-Al_2O_3 and Au-MgO interfaces [46] showing the effect of Ti oxidation on TBC. These studies focused on Ti because of its use as an adhesion layer for metal contacts. Our observations are in agreement with these studies and further broaden the notion of reduction in TBC due to oxidation to other metals as we compare the effect of different metals on TBC such as Ni in addition Ti. Further, the difference in metal and metal oxide Debye temperatures (Ti = 420 K [82], TiO_2 = 750 K [83], Ni = 495 K [84], NiO = 630 K [85]) suggests the chemical interaction plays a major role in the thermal transport at the M-G interface. The chemisorbed interface between graphene and metal may not be formed due to the thin native oxide layer in bottom Ti and Ni layer in our samples which could explain why high TBC was not observed as predicted by previous computational studies [31,35] even though conductance of oxide layer itself is much greater than the interfacial conductance (TBC).

In addition, the C1s XPS spectra for graphene on Ti and Ni showed no carbide formation at bottom interface which can also affect interfacial properties [86–88]. Gengler et al. [37] reported a decrease in TBC with increased titanium carbide concentration, but the absence of carbide formation in our samples leaves oxidation as the likely hindrance of M-G interaction at bottom interface. Further investigation is required to develop method which can reduce oxidation in Ti and Ni layers, such as selective etching of surface oxide layer or ultra-high vacuum metal deposition [46,89], and determine whether such reduction in oxidation will lead to significant enhancement in TBC. However, this explanation is not sufficient to show why Au sample had similar TBC indicating that the bonding interactions are not the only important consideration for dictating TBC in our samples since the physisorbed sample (Au) was slightly higher than one chemisorbed sample (Ni) but lower than the other (Ti). For example, interface topology has a major effect on M-G TBC [25]. Different deposition methods (e.g., evaporation, sputtering) and deposition conditions (e.g., rate, pressure) can affect the surface roughness of metal films and thus the topology of the M-G interface. The chemisorbed M-G interface is expected to change electronic configuration [19–21] as well as phonon dispersion [27–31] of graphene. Huang et al. [26] showed that thermal transport at Pd-G-Pd interfaces was due to phonons with no significant electronic contribution, which could also explain why no TBC enhancement was observed. Interestingly, the insertion of a single monolayer of graphene significantly reduces the TBC at Au-Au interface by more than two orders of magnitude. From this we can conclude the electronic contribution to TBC at M-M interfaces is negated by the presence of the graphene.

4. Conclusions

We have presented TBC measurements for Ti-G-Ti, Ni-G-Ni, and Au-G-Au interfaces using TDTR which represent chemisorbed (Ti, Ni) and physisorbed (Au) interfaces based on how these metals interact with graphene. The TBC at these interfaces were similar to previously reported TBC at M-G-SiO_2 and M-G-M interfaces. Oxidation of the bottom Ti (2.8 nm) and Ni layers (2.5 nm) was confirmed using XPS and led to decreased TBC at Ti-G-Ti and Ni-G-Ni interfaces by preventing the formation of chemisorbed interface between graphene and metal. Reducing the oxidation of the bottom Ti and Ni layers should lead to enhanced TBC, a necessary consideration for fabrication of future graphene devices. The results of this study also show insertion of one monolayer of graphene can significantly reduce thermal transport at metal-metal interface with no oxidation (e.g., Au-Au).

Acknowledgements

This work was partially supported by National Science Foundation Grant CBET-1236416. D.B.B. was supported by a National Science Foundation Graduate Research Fellowship under Grant No. DGE-1650044. Any opinion, findings, and conclusions or recommendations expressed in this material are those of the authors and do not necessarily reflect the views of the National Science Foundation.

References

[1] K.S. Novoselov, et al., Electric field effect in atomically thin carbon films, Science 306 (5696) (2004) 666–669.
[2] Y.B. Zhang, et al., Experimental observation of the quantum Hall effect and Berry's phase in graphene, Nature 438 (7065) (2005) 201–204.
[3] K.S. Novoselov, et al., Two-dimensional gas of massless Dirac fermions in graphene, Nature 438 (7065) (2005) 197–200.
[4] C. Berger, et al., Electronic confinement and coherence in patterned epitaxial graphene, Science 312 (5777) (2006) 1191–1196.
[5] K.I. Bolotin, et al., Ultrahigh electron mobility in suspended graphene, Solid State Commun. 146 (9–10) (2008) 351–355.
[6] A.A. Balandin, et al., Superior thermal conductivity of single-layer graphene, Nano Lett. 8 (3) (2008) 902–907.
[7] S. Ghosh, et al., Extremely high thermal conductivity of graphene: prospects for thermal management applications in nanoelectronic circuits, Appl. Phys. Lett. 92 (15) (2008).
[8] W.W. Cai, et al., Thermal transport in suspended and supported monolayer graphene grown by chemical vapor deposition, Nano Lett. 10 (5) (2010) 1645–1651.
[9] M.C. Lemme, et al., A graphene field-effect device, IEEE Electron. Device Lett. 28 (4) (2007) 282–284.
[10] Y.M. Lin, et al., 100-GHz transistors from Wafer-scale epitaxial graphene, Science 327 (5966) (2010) 662, 662.
[11] F.N. Xia, et al., Ultrafast graphene photodetector, Nat. Nanotechnol. 4 (12) (2009) 839–843.
[12] T. Mueller, F.N.A. Xia, P. Avouris, Graphene photodetectors for high-speed optical communications, Nat. Photon. 4 (5) (2010) 297–301.
[13] E. Pop, et al., Electrical and thermal transport in metallic single-wall carbon nanotubes on insulating substrates, J. Appl. Phys. 101 (9) (2007).
[14] A.D. Liao, et al., Thermally limited current carrying ability of graphene nanoribbons, Phys. Rev. Lett. 106 (25) (2011).
[15] P.L. Kapitza, Heat transfer and superfluidity of helium II, J. Phys.-USSR 5 (1–6) (1941) 59–69.
[16] E.T. Swartz, R.O. Pohl, Thermal-boundary resistance, Rev. Mod. Phys. 61 (3) (1989) 605–668.
[17] E. Pop, Energy dissipation and transport in nanoscale devices, Nano Research 3 (3) (2010) 147–169.
[18] J.X. Zheng, et al., Interfacial properties of bilayer and trilayer graphene on metal substrates, Sci. Rep. 3 (2013).
[19] G. Giovannetti, et al., Doping graphene with metal contacts, Phys. Rev. Lett. 101 (2) (2008).
[20] P.A. Khomyakov, et al., First-principles study of the interaction and charge transfer between graphene and metals, Phys. Rev. B 79 (19) (2009).
[21] B.J. Schultz, et al., On chemical bonding and electronic structure of graphene-metal contacts, Chem. Sci. 4 (1) (2013) 494–502.
[22] V.V. Cheianov, V.I. Fal'ko, Selective transmission of Dirac electrons and ballistic magnetoresistance of n-p junctions in graphene, Phys. Rev. B 74 (4) (2006).
[23] C.H. Park, et al., Anisotropic behaviours of massless Dirac fermions in graphene under periodic potentials, Nat. Phys. 4 (3) (2008) 213–217.
[24] Y.K. Koh, et al., Heat conduction across monolayer and few-layer graphenes, Nano Lett. 10 (11) (2010) 4363–4368.
[25] B. Huang, Y.K. Koh, Improved topological conformity enhances heat conduction across metal contacts on transferred graphene, Carbon 105 (2016) 268–274.
[26] B. Huang, Y.K. Koh, Negligible electronic contribution to heat transfer across intrinsic metal/graphene interfaces, Advanced Materials Interfaces 4 (20) (2017).
[27] T. Aizawa, et al., Phonon-dispersion in monolayer graphite formed on Ni(111) and Ni(001), Surf. Sci. 237 (1–3) (1990) 194–202.
[28] T. Aizawa, et al., Phonon-dispersion of monolayer graphite on Pt(111) and nbc surfaces - bond softening and interface structures, Surf. Sci. 260 (1–3) (1992) 311–318.
[29] A. Allard, L. Wirtz, Graphene on metallic substrates: suppression of the Kohn anomalies in the phonon dispersion, Nano Lett. 10 (11) (2010) 4335–4340.
[30] L. Chen, Z. Huang, S. Kumar, Phonon transmission and thermal conductance across graphene/Cu interface, Appl. Phys. Lett. 103 (12) (2013).
[31] L. Chen, Z. Huang, S. Kumar, Impact of bonding at multi-layer graphene/metal Interfaces on thermal boundary conductance, RSC Adv. 4 (68) (2014) 35852–35861.
[32] A.M. Shikin, et al., Surface phonon dispersion of a graphite monolayer adsorbed on Ni(111) and its modification caused by intercalation of Yb, La and Cu layers, Surf. Sci. 424 (1) (1999) 155–167.
[33] C. Gong, et al., Metal-graphene-metal sandwich contacts for enhanced interface bonding and work function control, ACS Nano 6 (6) (2012) 5381–5387.
[34] A.D. Franklin, et al., Double contacts for improved performance of graphene transistors, IEEE Electron. Device Lett. 33 (1) (2012) 17–19.
[35] R. Mao, et al., First-principles calculation of thermal transport in metal/graphene systems, Phys. Rev. B 87 (16) (2013).
[36] A.J. Schmidt, et al., Thermal conductance and phonon transmissivity of metal-graphite interfaces, J. Appl. Phys. 107 (10) (2010).
[37] J.J. Gengler, et al., Limited thermal conductance of metal-carbon interfaces, J. Appl. Phys. 112 (9) (2012).
[38] P.E. Hopkins, et al., Manipulating thermal conductance at metal-graphene contacts via chemical functionalization, Nano Lett. 12 (2) (2012) 590–595.
[39] J. Yang, et al., Thermal conductance imaging of graphene contacts, J. Appl. Phys. 116 (2) (2014).
[40] B.M. Foley, et al., Modifying surface energy of graphene via plasma-based chemical functionalization to tune thermal and electrical transport at metal interfaces, Nano Lett. 15 (8) (2015) 4876–4882.
[41] S.G. Walton, et al., Plasma-based chemical functionalization of graphene to control the thermal transport at graphene-metal interfaces, Surf. Coating. Technol. 314 (2017) 148–154.
[42] F. Keren, et al., Titanium contacts to graphene: process-induced variability in electronic and thermal transport, Nanotechnology (2018).
[43] T. Jiang, et al., Covalent bonding modulated graphene-metal interfacial thermal transport, Nanoscale 8 (21) (2016) 10993–11001.
[44] C.W. Zhang, et al., Electron contributions to the heat conduction across Au/graphene/Au interfaces, Carbon 115 (2017) 665–671.
[45] M.D. Losego, et al., Effects of chemical bonding on heat transport across interfaces, Nat. Mater. 11 (6) (2012) 502–506.
[46] D.H. Olson, et al., The influence of titanium adhesion layer oxygen stoichiometry on thermal boundary conductance at gold contacts, Appl. Phys. Lett. 112 (17) (2018).
[47] X.S. Li, et al., Transfer of large-area graphene films for high-performance transparent conductive electrodes, Nano Lett. 9 (12) (2009) 4359–4363.
[48] N. Liu, et al., The origin of wrinkles on transferred graphene, Nano Research 4 (10) (2011) 996–1004.
[49] X.S. Li, et al., Large-area synthesis of high-quality and uniform graphene films on copper foils, Science 324 (5932) (2009) 1312–1314.
[50] A. Pirkle, et al., The effect of chemical residues on the physical and electrical properties of chemical vapor deposited graphene transferred to SiO_2, Appl. Phys. Lett. 99 (12) (2011).
[51] Y.C. Lin, et al., Graphene annealing: how clean can it Be? Nano Lett. 12 (1) (2012) 414–419.
[52] B. Singh, N.A. Surplice, Electrical resistivity and resistance-temperature characteristics of thin titanium films, Thin Solid Films 10 (2) (1972) 243–&.
[53] P.E. Friebertshauser, J.W. Mccamont, Electrical properties of titanium zirconium and hafnium films from 300 degrees K to 1.3 degrees K, J. Vac. Sci. Technol. 6 (1) (1969) 184–+.
[54] B.C. Gundrum, D.G. Cahill, R.S. Averback, Thermal conductance of metal-metal interfaces, Phys. Rev. B 72 (24) (2005).
[55] R.B. Wilson, D.G. Cahill, Experimental validation of the interfacial form of the Wiedemann-Franz law, Phys. Rev. Lett. 108 (25) (2012).
[56] N.W. Ashcroft, N.D. Mermin, Solid State Physics, Holt. xxi, New York, 1976, p. 826.
[57] T.L. Bougher, et al., Thermal boundary resistance in GaN films measured by time domain thermoreflectance with robust Monte Carlo uncertainty estimation, Nanoscale Microscale Thermophys. Eng. 20 (1) (2016) 22–32.
[58] D.G. Cahill, Analysis of heat flow in layered structures for time-domain thermoreflectance, Rev. Sci. Instrum. 75 (12) (2004) 5119–5122.
[59] J. Liu, et al., Simultaneous measurement of thermal conductivity and heat capacity of bulk and thin film materials using frequency-dependent transient thermoreflectance method, Rev. Sci. Instrum. 84 (3) (2013).
[60] W.H. Press, Numerical Recipes : the Art of Scientific Computing, third ed., Cambridge University Press. xxi, Cambridge, UK ; New York, 2007, p. 1235.
[61] Y.K. Koh, D.G. Cahill, Frequency dependence of the thermal conductivity of semiconductor alloys, Phys. Rev. B 76 (7) (2007).
[62] P.E. Hopkins, et al., Criteria for cross-plane dominated thermal transport in multilayer thin film systems during modulated laser heating, Journal of Heat Transfer-Transactions of the Asme 132 (8) (2010).
[63] A.J. Schmidt, X.Y. Chen, G. Chen, Pulse accumulation, radial heat conduction, and anisotropic thermal conductivity in pump-probe transient thermoreflectance, Rev. Sci. Instrum. 79 (11) (2008).
[64] J. Yang, E. Ziade, A.J. Schmidt, Uncertainty analysis of thermoreflectance measurements, Rev. Sci. Instrum. 87 (1) (2016).
[65] P.Q. Jiang, X. Qian, R.G. Yang, Time-domain thermoreflectance (TDTR) measurements of anisotropic thermal conductivity using a variable spot size approach, Rev. Sci. Instrum. 88 (7) (2017).
[66] C.W. Nan, et al., Effective thermal conductivity of particulate composites with interfacial thermal resistance, J. Appl. Phys. 81 (10) (1997) 6692–6699.
[67] A.C. Ferrari, et al., Raman spectrum of graphene and graphene layers, Phys. Rev. Lett. 97 (18) (2006).
[68] F. Tuinstra, J.L. Koenig, Raman spectrum of graphite, J. Chem. Phys. 53 (3) (1970) 1126–&.
[69] A.C. Ferrari, J. Robertson, Interpretation of Raman spectra of disordered and amorphous carbon, Phys. Rev. B 61 (20) (2000) 14095–14107.
[70] L.G. Cancado, et al., Quantifying defects in graphene via Raman spectroscopy at different excitation energies, Nano Lett. 11 (8) (2011) 3190–3196.
[71] Purdue University Thermophysical Properties Research Center, Y.S. Touloukian, Thermophysical Properties of Matter; [the TPRC Data Series; a Comprehensive Compilation of Data, IFI/Plenum, New York, 1970.
[72] G.S. Kumar, G. Prasad, R.O. Pohl, Experimental determinations of the Lorenz number, J. Mater. Sci. 28 (16) (1993) 4261–4272.
[73] P.E. Hopkins, et al., Effects of surface roughness and oxide layer on the thermal boundary conductance at aluminum/silicon interfaces, Phys. Rev. B 82 (8) (2010).
[74] E. McCafferty, J.P. Wightman, An X-ray photoelectron spectroscopy sputter

profile study of the native air-formed oxide film on titanium, Appl. Surf. Sci. 143 (1–4) (1999) 92–100.
[75] Jablonski, C.J.P.a.A., NIST Electron Inelastic-mean-free-path Database - Version 1.2. 2010, Gaithersburg, MD: National Institute of Standards and Technology.
[76] W.H. Gries, A universal predictive equation for the inelastic mean free path-lengths of x-ray photoelectrons and Auger electrons, Surf. Interface Anal. 24 (1) (1996) 38–50.
[77] H.W. Nesbitt, D. Legrand, G.M. Bancroft, Interpretation of Ni2p XPS spectra of Ni conductors and Ni insulators, Phys. Chem. Miner. 27 (5) (2000) 357–366.
[78] B.R. Strohmeier, An esca method for determining the oxide thickness on aluminum-alloys, Surf. Interface Anal. 15 (1) (1990) 51–56.
[79] B.P. Payne, et al., Structure and growth of oxides on polycrystalline nickel surfaces, Surf. Interface Anal. 39 (7) (2007) 582–592.
[80] M.C. Biesinger, et al., X-ray photoelectron spectroscopic chemical state quantification of mixed nickel metal, oxide and hydroxide systems, Surf. Interface Anal. 41 (4) (2009) 324–332.
[81] S.M. Lee, D.G. Cahill, Influence of interface thermal conductance on the apparent thermal conductivity of thin films, Microscale Thermophys. Eng. 1 (1) (1997) 47–52.
[82] C. Kittel, Introduction to Solid State Physics, eighth ed., Wiley. xix, Hoboken, NJ, 2005, p. 680.
[83] H.N. Pandey, The theoretical elastic constants and specific heats of rutile, Phys. Status Solidi 11 (2) (1965) 743–751.
[84] P.K. George, E.D. Thompson, Debye temperature of nickel from 0 to 300 degrees K, J. Phys. Chem. Solid. 28 (12) (1967) 2539–&.
[85] R.A. Coy, C.W. Tompson, E. Gurmen, Phonon dispersion in nio, Solid State Commun. 18 (7) (1976) 845–847.
[86] W.P. Leroy, et al., Solid-state formation of titanium carbide and molybdenum carbide as contacts for carbon-containing semiconductors, J. Appl. Phys. 99 (6) (2006).
[87] B. Huard, et al., Evidence of the role of contacts on the observed electron-hole asymmetry in graphene, Phys. Rev. B 78 (12) (2008).
[88] M. Politou, et al., Transition metal contacts to graphene, Appl. Phys. Lett. 107 (15) (2015).
[89] C.D. English, et al., Improved contacts to MoS2 transistors by ultra-high vacuum metal deposition, Nano Lett. 16 (6) (2016) 3824–3830.